Clay Minerals, (2012) **47**, 45–58

Mineralogical characteristics and geological significance of Albian (Early Cretaceous) glauconite in Zanda, southwestern Tibet, China

XIANG LI[1], YUANFENG CAI[2,*], XIUMIAN HU[2], ZHICHENG HUANG[2] AND JIANGANG WANG[2]

[1] *Wuhan Institute of Geology and Mineral Resources, China Geological Survey, Wuhan 430223, China, and* [2] *State Key Laboratory for Mineral Deposits Research (Nanjing University), School of Earth Sciences and Engineering, Nanjing University, Nanjing 210093, China*

(*Received 27 November 2010; revised 9 September 2011; Editor: George Christidis*)

ABSTRACT: Early Cretaceous glauconite from the Xiala section, southwestern Tibet, China, was investigated by petrographic microscopy and scanning electron microscopy (SEM), X-ray diffractometry (XRD), Fourier transform infrared (FTIR) spectroscopy, and electron probe microanalysis (EPMA). The investigations revealed that the glauconite in both sandstones and limestone is highly evolved. The glauconite in sandstone is autochthonous, but in limestone it may be derived from the underlying glauconitic sandstone. Based on analyses of the depositional environments and comparisons of glauconite-bearing strata in Zanda with sequences in adjacent areas, we conclude that the glauconitization at Zanda was probably associated with rising sea levels during the Late Albian, which represent the final separation of the Indian continent from the Australian-Antarctic continent. After the separation of the Indian continent from the Australian-Antarctic continent, cooling of the Indian continent resulted in subsidence and northward subduction of the Indian plate. A gradually rising sea level in Zanda, located along the northern margin of the Indian continent, was the cause of the low sedimentation rate. Continued transgression resulted in the occurrence of the highly evolved glauconite in this area.

KEYWORDS: glauconite, mineralogical characteristics, geological implication, Xiala section, Zanda, Tibet.

Glauconite is a micaceous clay mineral rich in iron but depleted in magnesium and aluminum; its K_2O content is generally high (>6%) (Odin & Matter, 1981; Odom, 1984; Stille & Clauer, 1994; Eder *et al.*, 2007) but is lower than that of mica-group minerals. Glauconite is considered an important "facies mineral" because of its mode of occurrence and its chemical composition (Chen, 1980; Vail *et al.*, 1984; Loutit *et al.*, 1988; Posamentier *et al.*, 1988; Amorosi, 1995, 1997). Generally, it is considered to form near the sediment-sea water interface under conditions of very low sedimentation rates (Odin & Matter, 1981; Amorosi, 1997; Kelly & Webb, 1999; Wiewióra *et al.*, 2001; Jiménez-Millán & Castro, 2008; Huggett *et al.*, 2010). Glauconite-bearing strata, which are characteristic of condensed sections (i.e. reflecting low sedimentation rates), are generally associated with transgressive sequences (Baum & Vail, 1988; Van Wagoner *et al.*, 1990; Amorosi, 1995; Berra *et al.*, 2007).

* E-mail: caiyf@nju.edu.cn
DOI: 10.1180/claymin.2012.047.1.45

Glauconite can be genetically classified as either autochthonous or allochthonous (Amorosi, 1997). Allochthonous glauconite is introduced into sediments from external sources, such as reworking of glauconite grains from older strata. Autochthonous glauconite, on the other hand, forms *in situ* and bears the signature of the physicochemical, sedimentological, and palaeo-oceanographic conditions that prevailed during the time of its formation (Kazakov, 1983; Stille & Clauer, 1994). Thus, the study of autochthonous glauconite can reveal information about the palaeoenvironmental conditions at the time of sediment deposition.

A suite of Early Cretaceous glauconite-bearing clastic rocks is exposed in the Xiala section of Zanda, southwestern Tibet, China (Fig. 1). In this paper we describe our investigations of the morphology, physical appearance and chemical

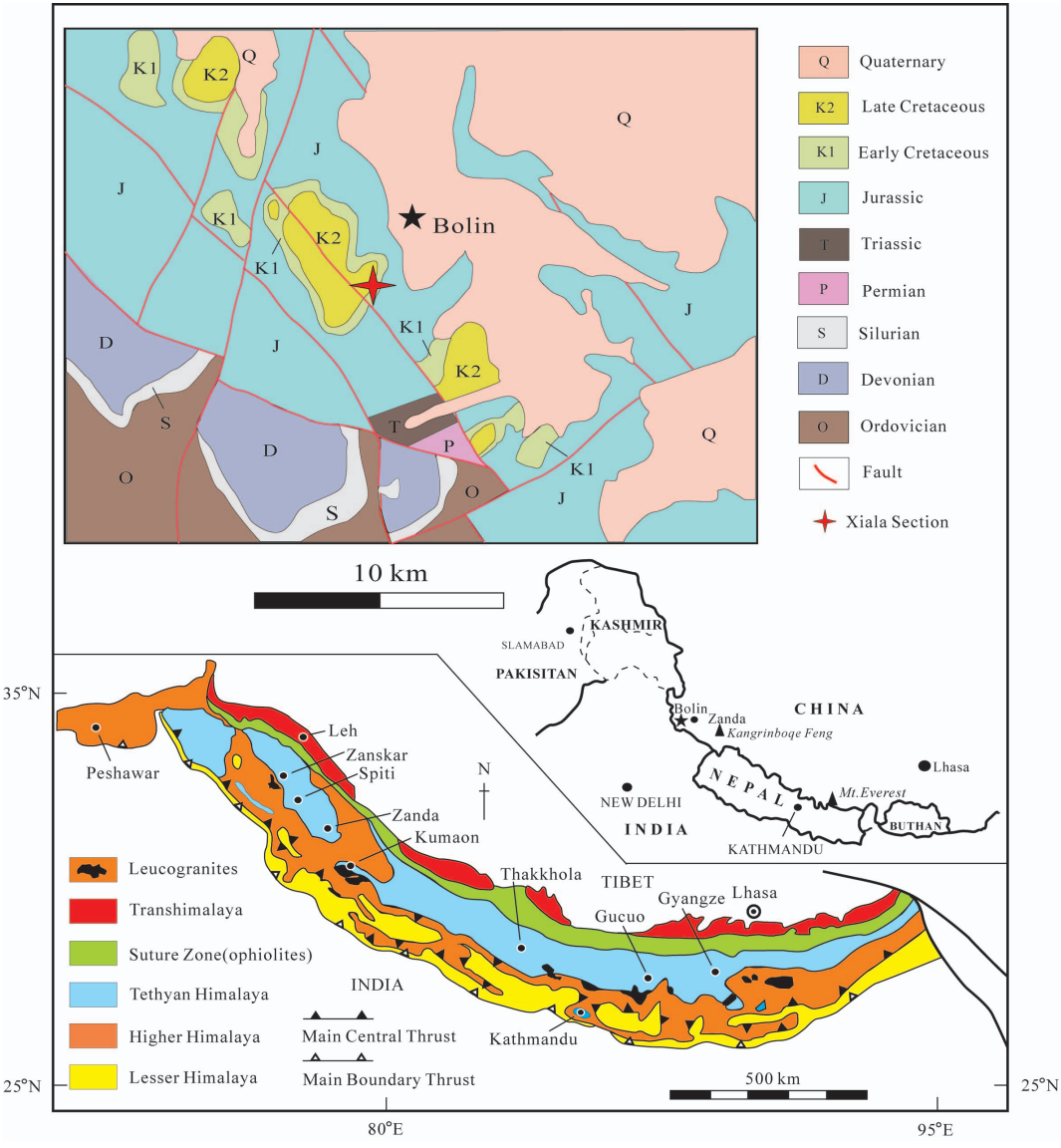

FIG. 1. Geological sketch map of the central Himalayan region showing the tectonic setting and location of the Xiala section, Bolin, Zanda (modified from Dèzes, 1999).

composition of glauconite in the Xiala section, with the aim of determining its origin and clarifying the geological conditions of its formation. We also discuss the depositional environment in which the glauconite formed, to further constrain the mechanisms and conditions of glauconite formation.

GEOLOGICAL SETTING

The Himalayan orogenic belt is the result of the convergence and collision of the Indian and Asian plates. Major litho-tectonic units in the belt are oriented east–west or southeast–northwest, and are laterally continuous over a broad region. From north to south, these litho-tectonic units are the Gangdese magmatic arc, the Xigaze forearc basin, the Yarlung Zangbo suture zone, the Tethys Himalayan zone, the Higher Himalayan zone, and the Lesser Himalayan zone (Fig. 1). The Yarlung Zangbo suture zone, which marks the contact between the Indian and Asian plates, consists of ophiolitic rocks and tectonic mélanges in a matrix of mud or serpentine (Hébert *et al.*, 2003; Dubois-Côté *et al.*, 2005; Dupuis *et al.*, 2005a, b, 2006; Bédard *et al.*, 2009). Southward, the Higher Himalayan metamorphic rocks are separated from the Lesser Himalayan zone by the Main Central Thrust (MCT) (Hodges *et al.*, 1996).

The Tethys Himalayan zone, composed of Palaeozoic to Eocene carbonates and clastic rocks (Garzanti, 1999; Jadoul *et al.*, 1998), is located between the Yarlung Zangbo suture zone and the Higher Himalayan zone, and represents sediments deposited on the northern margin of the Indian continent during the Cretaceous (Hodges, 2000). The Tethys Himalayan zone is further subdivided into southern and northern subzones. The southern subzone is characterized by the presence of shallow-water (shelf) calcareous and terrigenous sedimentary rocks of Palaeozoic to Eocene age (Liu & Einsele, 1994; Willems *et al.*, 1996; Hu *et al.*, 2010), whereas the northern subzone is dominated by Mesozoic to Palaeogene deep-water sedimentary deposits of the outer shelf, continental slope, and rise (Liu & Einsele, 1994; Hu *et al.*, 2008, 2010).

Here, we present data on a suite of Early Cretaceous glauconite-bearing clastic rocks belonging to the southern subzone of the Tethys Himalayan zone, in the Xiala section from Zanda, southwestern Tibet, China. The Xiala section is located 10 km east of the village of Bolin, in the Zanda basin (79º29′37.7″E, 31º16′16.2″N). The Cretaceous sequence in the Xiala section begins with clastic rocks of the Gajie Formation and is capped by pelagic limestones of the overlying Bolinxiala Formation (Guo *et al.*, 1991). In the lower part of the Gajie Formation, the strata are composed of lith-arenite and lithic quartz-arenite, with a transition to shales and silty shales in the middle part of the formation. The upper part of the formation is dominated by silty shales and subordinate lithic sandstones and lithic quartz sandstones. These strata were probably deposited in a delta-prodelta environment. The presence of Lower Cretaceous clastic rocks (similar to those of the Gajie Formation) has been documented at several localities on the northern margin of the palaeo-Indian continent, including at Zanskar, Spiti, Kumaon, Thakkhola, and Gucuo (Fig. 1) (Sinha, 1989; Garzanti, 1993, 1999; Gibling *et al.*, 1994; Chen *et al.*, 2007; Li *et al.*, 2009; Hu *et al.*, 2010).

A glauconite-bearing condensed section located at the contact between the Gajie and Bolinxiala formations consists of a glauconitic sandstone several tens of centimetres thick in the uppermost Gajie Formation, and a glauconite-bearing 1m thick limestone at the base of the Bolinxiala Formation.

The Bolinxiala Formation is composed of medium- to thick-bedded limestone partly intercalated with marlite, and the presence of abundant planktonic foraminifera (Li *et al.*, 2009), indicating that the formation was deposited in a pelagic environment. Assemblages of planktonic foraminifera in the Xiala section indicate that the Bolinxiala Formation is Late Albian to Maastrichtian in age. On the basis of lithologies and fossil assemblages, the Bolinxiala Formation can be correlated with the Chikkim Formation in the Spiti area (Fig. 1) (Bertle & Suttner, 2005). Planktonic foraminifera from samples XL33 and XL34 define the *Rotalipora ticinensis* zone, suggesting a Late Albian age for these strata (Li *et al.*, 2009).

MATERIALS AND METHODS

Three samples were collected from the Xiala section: two samples of glauconitic sandstone XL33 and XL34 from the Gajie Formation, and one sample of glauconite-bearing limestone XL35 from the Bolinxiala Formation (Fig. 2).

Polished thin sections were prepared for investigations by polarizing optical microscope, scanning electron microscope (SEM), and electron probe micro-analyser (EPMA). The SEM observations

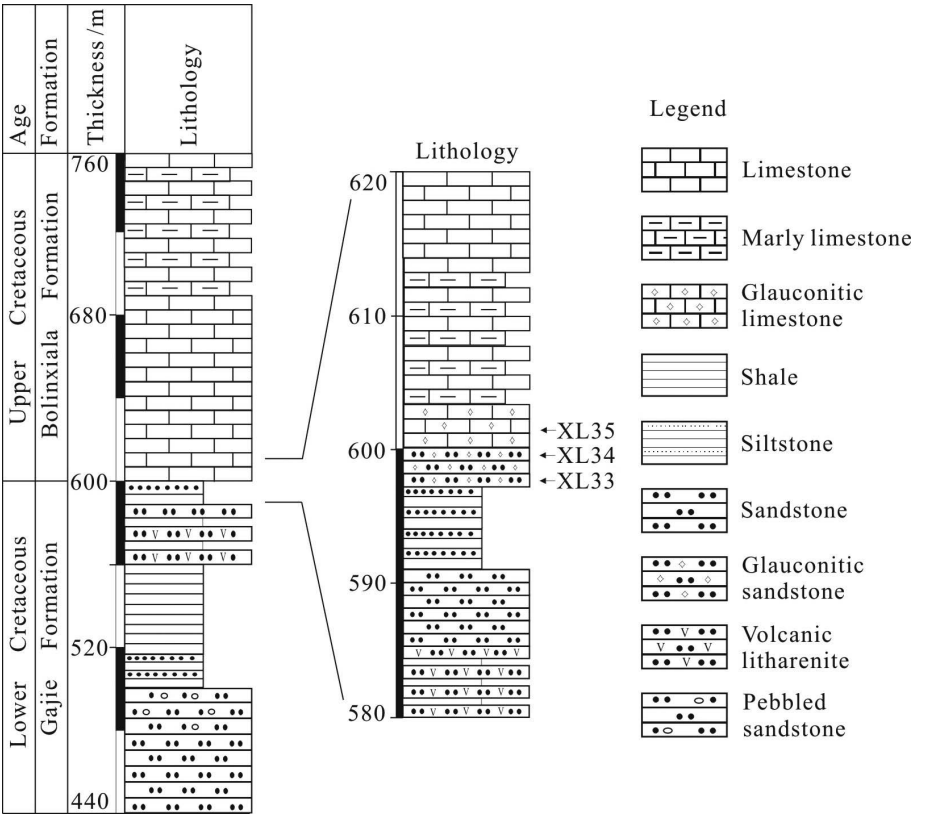

FIG. 2. Stratigraphy and petrography of the Xiala section, Bolin, Zanda, showing sample locations.

were conducted using a JEOL-6490 SEM equipped with an energy dispersive spectrometer (EDS), operated at an acceleration voltage of 20 kV. The EPMA was conducted using a JEOL JXA-8100, operated at an acceleration voltage of 15 kV and a beam current of 20 nA. The beam diameter was narrowed to less than 1 μm for the chemical analyses.

The glauconite grains were separated from the rocks and purified as follows. Disaggregated samples were passed through a 65 mesh screen and rinsed with distilled water. Glauconite grains were separated from quartz and calcite using a magnetic separator and were hand-picked from the magnetic separate under a binocular microscope. Finally, the selected fraction was ground to 200 mesh.

X-ray diffraction (XRD) analyses were conducted using a Rigaku D/Max-IIIa diffractometer equipped with a Cu target tube and a curved graphite monochromator, operated at 37.5 kV and 20 mA. Divergence and scattering slits on the system were 1º, and the receiving slit was 0.3 mm. Samples were step-scanned from 3º to 70º, with a step size of 0.02º (2θ) and a preset time of 2 s/step. Random powder mounts were prepared using the side-packing method suggested by the National Bureau of Standards, USA. Fourier transform infrared (FTIR) spectra were obtained using a NEXUS 870 spectrometer. Purified glauconite (5 mg) was added to, and homogeneously mixed with 495 mg of KBr. Then 200 mg of the resulting mixture were pressed into a 13 mm pellet. The pellet was placed into a vacuum oven and heated at 100ºC for 24 h to remove most of the absorbed water. Absorption intensities were recorded from 400 to 4000 cm^{-1} at 1 cm^{-1} intervals.

The glauconite grains purified from sample XL34 were also analysed by X-ray fluorescence (XRF) spectroscopy using an ARL-9800 spectrometer. The Fe_2O_3 and FeO contents of the glauconites were determined by oxidation-reduction titration.

All analyses described above were conducted at the State Key Laboratory of Mineral Deposits Research, and the Center of Modern Analysis, Nanjing University, China.

RESULTS

Optical and SEM microscopy

Examination of thin sections by petrographic microscope revealed that glauconite in the condensed section occurs as diverse grains, matrix, and pseudomorphs after other minerals. The sizes of grains range from several tens to several hundreds of micrometres. The colour of glauconite is predominately dark green in grains and light green in the matrix. Under cross-polarized light, the glauconite grains are cryptocrystalline and display aggregate polarization (Fig. 3a).

The glauconitic sandstone (samples XL33 and XL34) contains 30–40% glauconite grains; the grains are dark green and show irregular forms varying from rounded to subangular. Some grains display obvious fractures, attributed to either expansion of the glauconite grains or to partial desiccation during glauconitization (McRae, 1972). A few grains show notched, toothed, or lacerated margins (Fig. 3b). Sparry calcite is widely present as rims on the glauconite grains, with growth directions perpendicular to the edges of grains. At the contacts between glauconite grains and pre-existing calcite grains, glauconite replaces calcite along cleavage fractures (Fig. 3c). Glauconite also fills inter-grain fractures and micropores caused by dissolution of quartz (Fig. 3d).

In the limestone (sample XL35), the glauconite content is less than 10% by volume. In thin sections, glauconite grains are inhomogeneously dispersed and concentrated in places. Quartz grains show distribution patterns similar to those of glauconite, suggesting that they are both reworked (Fig. 3e). Glauconite grains show low sphericities and are poorly graded, indicating that the grains did not undergo long-distance transport. Iron oxide particles and halos around glauconite are also common in the matrix (Fig. 3f).

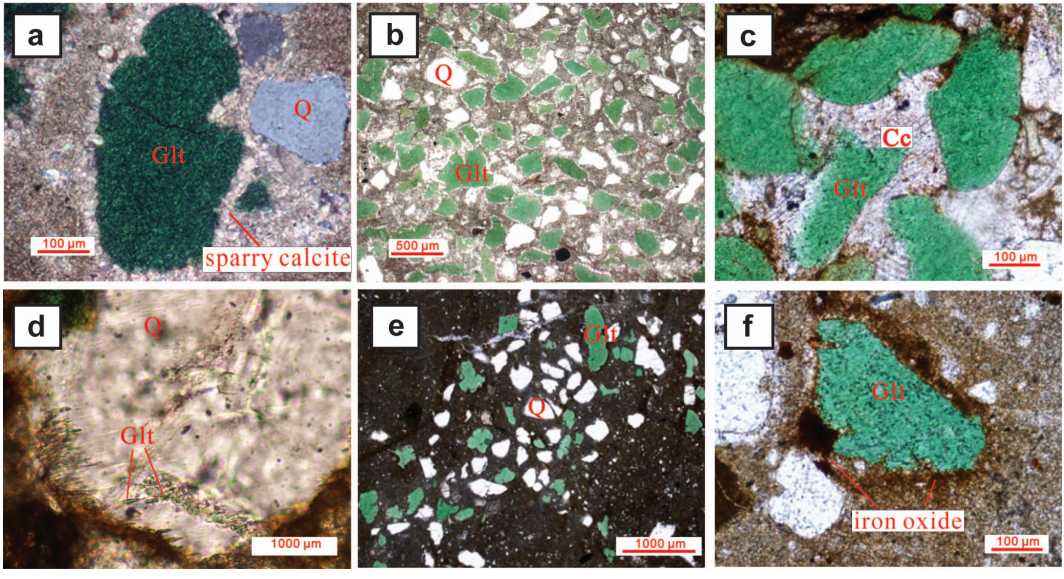

FIG. 3. Photomicrographs of Cretaceous (Albian) glauconites at Zanda, southwestern Tibet. (a) Glauconite in microcrystalline aggregate form, cemented by sparry calcite (glauconitic sandstone, XL33, cross-polarized light). (b) Different forms of glauconite cemented by sparry calcite (glauconitic sandstone, XL33). (c) Glauconite replacing calcite along cleavages (glauconitic sandstone, XL34). (d) Micropores in quartz in-filled by glauconite precursors (glauconitic sandstone, XL34). (e) Glauconite and quartz locally concentrated as ribbons (limestone, XL35). (f) Iron oxide particles or halos around glauconite (limestone, XL35). Glt, glauconite; Cc, calcite; Q, Quartz.

SEM images show that aggregates of glauconite grains consist of flaky particles ranging in size from 1 to 3 μm. Glauconite particles can be divided into two habits on the basis of structural properties. In one habit, the particles are bent and curled, and gaps along crystal boundaries result in high porosities (Fig. 4a); this habit is common along the margins of grains exposed to open growth space. The second habit is marked by the presence of compactly arranged particles, and occurs along grains exposed to narrow growth space (Fig. 4b). Both habits are characteristic of highly evolved glauconite grains, as described by Odin & Matter (1981). The glauconite in sandstones and limestones frequently occurs in the form of compact particles. Glauconite replaces calcite, although the extent of replacement is variable (Fig. 4c). Glauconite also fills fractures and cavities in quartz grains (Fig. 4d).

X-ray diffraction data

The evolution of glauconitic minerals, from less-ordered to more-ordered varieties, is reflected in the XRD patterns (Odin & Matter, 1981). Burst (1958a,b) proposed an X-ray classification of glauconitic minerals based on characteristic patterns of X-ray reflections. Figure 5 shows the XRD patterns of the three samples of purified glauconite analysed in this study. Sharp and symmetric diffraction lines occur at 10.018 Å (001), 4.516 Å (020), 3.329 Å (003), 2.579 Å (130), and 1.510 Å (060). The 001 reflection generally shows a fairly broad base, but possesses a sharp appearance only when the peak is situated at 10 Å. The well defined 10 Å diffraction line is characteristic of a low volume of intra-crystalline swelling layers. The $11\bar{2}$ and 112 reflections are indicators of an ordered 1*M*

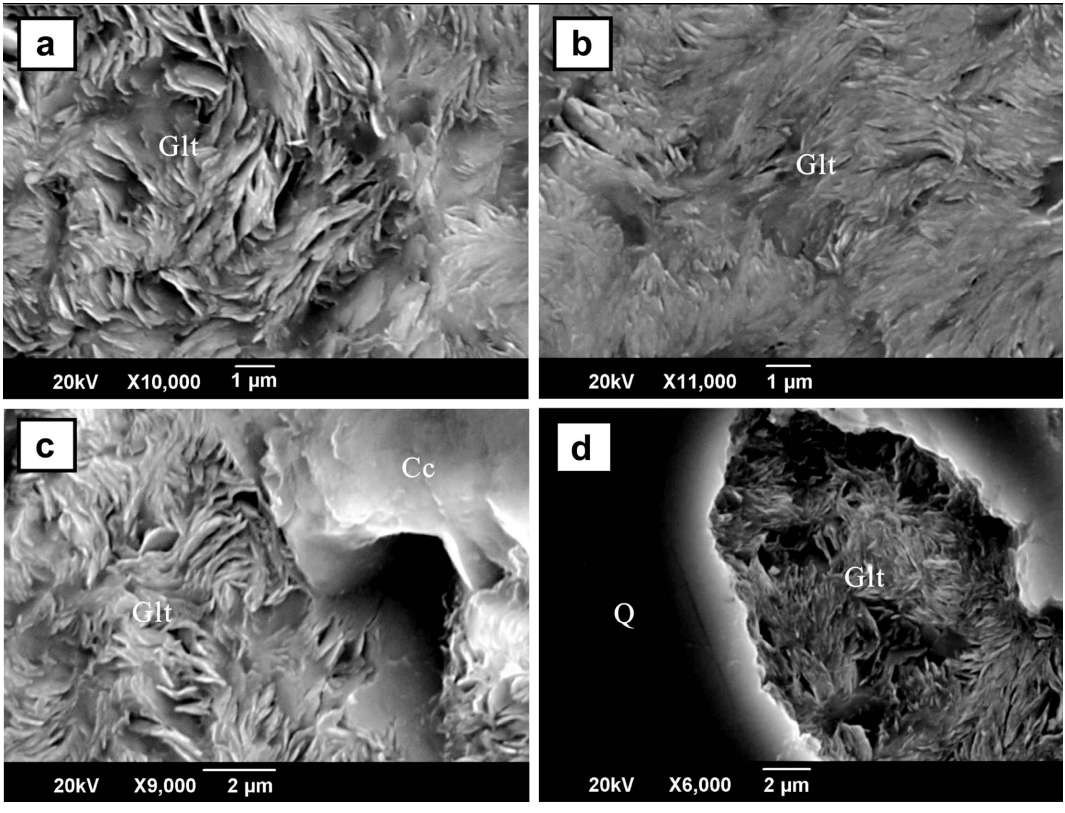

FIG. 4. SEM images of Cretaceous (Albian) glauconites at Zanda, southwestern Tibet. (a) Curved lamellar structure of glauconite (glauconitic sandstone, XL33). (b) Clustered aggregates of glauconite (glauconitic sandstone, XL33). (c) Replacement of calcite by glauconite along cleavages (glauconitic sandstone, XL34). (d) Micropores in quartz filled by glauconite (glauconitic sandstone, XL34). Abbreviations as in Fig. 3.

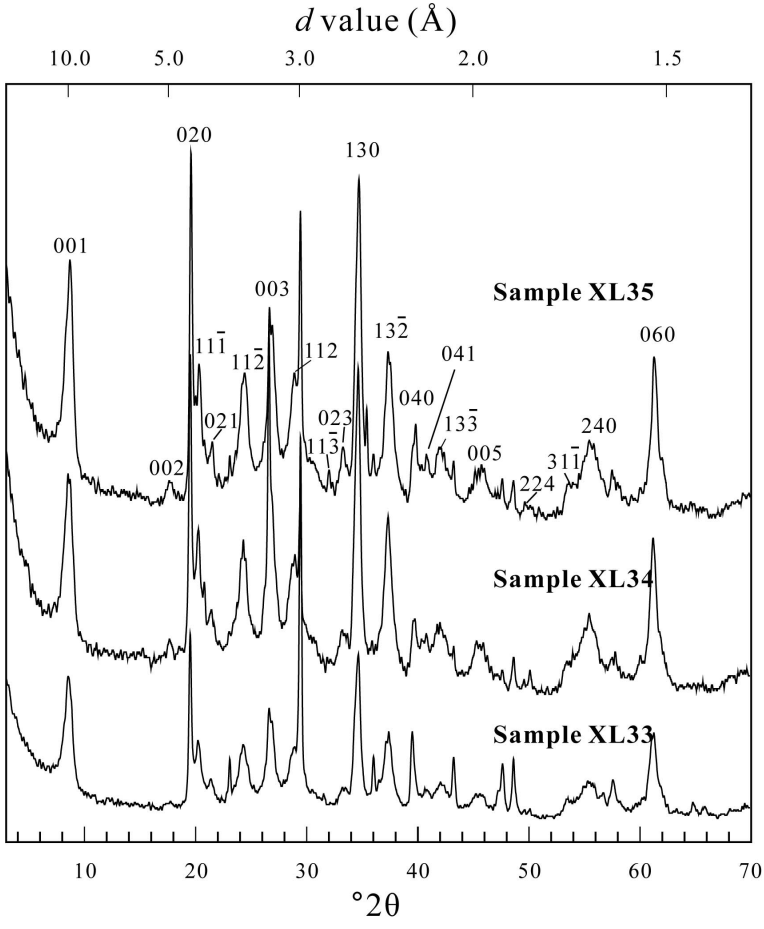

FIG. 5. XRD patterns of purified Cretaceous (Albian) glauconites from Zanda, southwestern Tibet.

structure for the layered silicate lattice structure (Bentor & Kastner, 1965; Odom, 1976; Chen, 1980; Zhang, 1981; Amouric & Parron, 1985). Table 1 compares the X-ray diffraction data from this study with published values of 1*M* structures of glauconite.

FTIR data

Figure 6 shows that the characteristic FTIR spectral bands for the three samples of purified glauconite (XL33–XL35) that occur in the OH-stretching vibration region (3400–3700 cm^{-1}) and the Si–O stretching vibration region (900–1100 cm^{-1}). In the high-wavenumber region, three absorption bands, centred at 3537.4, 3560.5, and 3603.1 cm^{-1}, can be attributed to the $Fe^{3+}Fe^{3+}$□OH, $AlFe^{2+}$□OH and AlMg□OH vibra-

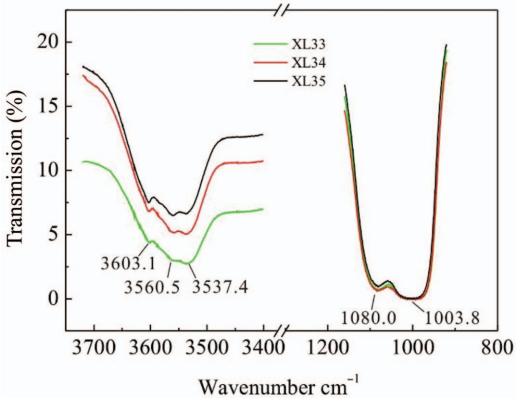

FIG. 6. FTIR spectra of purified Cretaceous (Albian) glauconites from Zanda, southwestern Tibet.

TABLE 1. Detailed X-ray diffraction data of Cretaceous (Albian) glauconites in sample XL35 from Zanda, southwestern Tibet, and detailed comparisons with published 1*M* glauconite structures.

	Glauconite-1M PDF 09-0439		Glauconite-1M (Zhang, 1981)		Glauconite This study	
hkl	*I*	*d*	*I*	*d*	*I*	*d*
001	100	10.1	9	10.03	74	10.018
002	1	4.98	3	4.98	9	5.007
020	80	4.53	5	4.53	98	4.516
11$\bar{1}$	20	4.35	1	4.36	37	4.350
021	10	4.12			4	4.125
11$\bar{2}$	40	3.63	4	3.67	35	3.613
003, 022	60	3.33	8	3.33	56	3.329
112	40	3.09	2	3.09	38	3.081
11$\bar{3}$	5	2.89	4	2.85	0.5	2.890
023	10	2.67			10	2.675
130, $\bar{1}$31, 200	100	2.587	10	2.583	100	2.579
13$\bar{2}$, 201	60	2.396	6	2.396	52	2.393
040, 22$\bar{1}$	20	2.263	2	2.264	17	2.259
220, 041	10	2.213	1	2.211	17	2.209
13$\bar{3}$, 202	20	2.154	1	2.138	13	2.151
005	20	1.994	3	1.992	15	1.993
224	5	1.817	2	1.815	0.5	1.817
31$\bar{1}$, 24$\bar{1}$	10	1.715	2	1.713	4	1.710
240, 31$\bar{2}$ (310, 241)	30	1.66	4	1.669	21	1.657
060, 33$\bar{1}$	60	1.511	9	1.518	48	1.510

tions, respectively (Besson & Drits, 1997a,b). The concentrations of octahedral cations can be approximated by the intensities of the OH vibration bands containing the given cations (Slonimskaya *et al.*, 1986; Besson & Drits, 1997a). The absorption intensities at 3537.4 cm^{-1} relative to those at 3603.1 cm^{-1} show a progressive decrease from samples XL33 to XL35, indicating that Fe^{3+} occupancy in the octahedra gradually decreases through time; Al contents, on the other hand, increase from samples XL33 to XL35.

In the Si–O stretching vibration region, two Si–O absorption bands are observed in the infrared (IR) spectrum of glauconites with low swelling-layer contents; only one Si–O band is observed in glauconites with high swelling-layer contents (Manghnani & Hower, 1964; Zhang, 1981). In our samples, two Si–O absorption bands occur in the 900–1100 cm^{-1} region. Based on the relationship between the positions of Si–O absorption bands near 1000 cm^{-1} and the concentrations of swelling layers (proposed by Manghnani & Hower, 1964), the concentrations of swelling layers in our glauconite samples are estimated to be less than 10%.

Chemical composition

Table 2 shows the results of microprobe analyses of glauconite grains purified from samples XL33, XL34 and XL35. Ten points on glauconite grains from each sample were randomly chosen for analysis, and the cation contents at different coordination sites were calculated on the basis of $O_{10}(OH)_2$.

The EPMA data (all in wt.%) show high average K_2O contents in glauconite from both glauconitic sandstone (XL33, Xl34) and glauconite-bearing limestone (XL35), with values of 7.87, 7.81 and 7.91%, respectively. Al_2O_3 contents are 9.60, 11.12 and 13.91%, respectively; Fe_2O_3 contents are 17.00, 15.37 and 12.38%, respectively; and FeO contents are 5.94, 5.37 and 4.33%, respectively. Relative to glauconite in sandstone, the glauconite in limestone shows higher average contents of Al_2O_3 (13.91% *vs.* 10.36%, respectively) and lower average contents of Fe_2O_3 (12.38% *vs.* 16.19%) and FeO (4.33% *vs.* 5.66%). In addition, there is no obvious relationship between ^{VI}Al and Fe^{3+} in glauconite from sandstone sample XL33 due to the presence of tetrahedral Al;

TABLE 2. EPMA data of Cretaceous (Albian) glauconites in samples XL33, XL34, and XL35 from Zanda, southwestern Tibet (analyses in wt.%).

	— XL33 (n = 10) —				— XL34 (n = 10) —				— XL35 (n = 10) —			
	Min.	Max.	Avg.	S.D.	Min.	Max.	Avg.	S.D.	Min.	Max.	Avg.	S.D.
SiO_2	48.15	52.88	51.31	1.65	50.81	54.61	53.02	1.32	52.60	56.19	54.55	1.35
TiO_2	0.09	0.28	0.21	0.05	0.10	0.26	0.17	0.05	0.08	0.18	0.13	0.03
Al_2O_3	8.47	10.66	9.60	0.65	9.44	13.01	11.12	1.23	11.82	16.01	13.91	1.30
Fe_2O_3	15.57	18.41	17.00	0.90	13.67	16.78	15.37	1.07	10.97	13.80	12.38	0.91
FeO	5.44	6.43	5.94	0.31	4.78	5.86	5.37	0.38	3.83	4.82	4.33	0.32
MgO	3.76	4.72	4.27	0.31	3.92	4.99	4.43	0.35	3.96	4.58	4.35	0.18
CaO	0.27	0.51	0.39	0.08	0.32	0.68	0.51	0.11	0.43	1.58	0.65	0.34
Na_2O	0.06	0.18	0.08	0.04	0.01	0.10	0.05	0.03	0.02	0.07	0.05	0.02
K_2O	6.93	8.30	7.87	0.40	7.34	8.10	7.81	0.31	7.56	8.23	7.91	0.23
Total	94.77	98.38	96.67	1.10	95.10	101.2	97.83	1.95	95.93	100.1	98.26	1.45
$Si_{a.p.f.u.}$	3.54	3.79	3.68	0.09	3.61	3.70	3.65	0.04	3.61	3.71	3.66	0.03
Ti	0.00	0.02	0.01	0.00	0.01	0.01	0.01	0.00	0.00	0.01	0.01	0.00
Al	0.20	0.45	0.31	0.09	0.29	0.39	0.35	0.03	0.28	0.38	0.33	0.03
^{IV}Al	0.35	0.61	0.50	0.09	0.46	0.69	0.56	0.08	0.65	0.89	0.77	0.08
Fe^{3+}	0.72	0.88	0.81	0.05	0.71	0.86	0.80	0.05	0.54	0.70	0.63	0.06
Fe^{2+}	0.33	0.39	0.36	0.02	0.28	0.33	0.31	0.02	0.21	0.27	0.24	0.02
Mg	0.40	0.51	0.46	0.03	0.40	0.52	0.45	0.03	0.41	0.46	0.44	0.02
$\Sigma^{VI}M$	2.00	2.30	2.13	0.09	2.07	2.15	2.11	0.03	2.05	2.10	2.08	0.02
Ca	0.02	0.04	0.03	0.01	0.02	0.05	0.04	0.01	0.03	0.12	0.05	0.02
Na	0.01	0.03	0.01	0.01	0.00	0.01	0.01	0.00	0.00	0.01	0.01	0.00
K	0.64	0.76	0.72	0.04	0.65	0.72	0.68	0.03	0.65	0.73	0.68	0.03
$\Sigma^{XII}A$	0.67	0.83	0.76	0.06	0.67	0.78	0.73	0.04	0.68	0.86	0.74	0.05

Notes: Min. = minimum; Max. = maximum; Avg. =average; S.D. = standard deviation
The Fe^{2+}: Fe^{3+} ratio in XL33 and XL35 is used as the ratio in XL34,which was obtained by oxidation−reduction titration

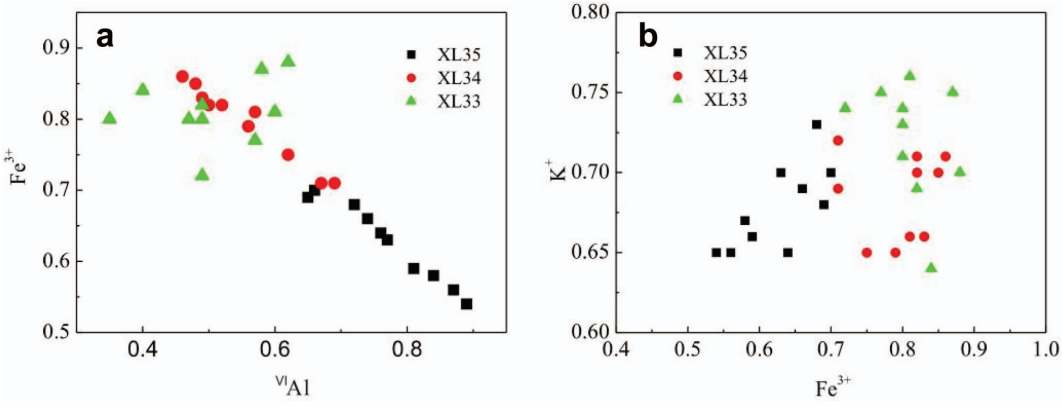

FIG. 7. (a) ^{VI}Al *vs.* Fe^{3+} in octahedra, and (b) K^+ *vs.* Fe^{3+} content plots, for samples of Cretaceous (Albian) glauconites from Zanda, southwestern Tibet.

however, ^{VI}Al and Fe^{3+} are negatively correlated in samples XL34 and XL35 (Fig. 7a). Interlayer K and octahedral Fe^{3+} in glauconite from the sandstone samples (XL33 and XL34) are not correlated; however, there is a weak positive correlation between interlayer K and octahedral Fe^{3+} in glauconite from limestone (sample XL35; Fig. 7b).

The sum of octahedrally coordinated cations ($\Sigma^{VI}M$) is 2.13 and 2.11 in sandstones and 2.08 in limestone; these values are close to the ideal dioctahedral value of 2.0. The average interlayer cation charges are 0.76 and 0.73 in sandstone, and 0.74 in limestone, consistent with the presence of less than 10% swelling layers in the glauconite (Thompson & Hower, 1975). XRF spectroscopy and oxidation-reduction titration analyses of glauconite grains from sandstone sample XL34 show Fe_2O_3 concentrations of 12.6% and FeO concentrations of 4.4%. The Fe^{2+}/TFe ratio of 31% is higher than usual (10−15%; Kuzmann *et al.*, 2008).

DISCUSSION

Maturity of glauconite

Autochthonous glauconite forms near the sediment-water interface. The precursor detrital clay progressively evolves toward an end member composed of a K-rich glauconitic mica (Odin & Matter, 1981; Odin & Fullagar, 1988). The process of glauconitization requires a low sedimentation rate, as high rates of sedimentation and rapid burial will terminate the process of glauconite formation. Therefore, the maturity of glauconite reflects the residence time of glauconite at the sediment-water interface (before burial), and glauconite evolution is generally related to the duration of hiatuses in sedimentation (Odin & Matter, 1981).

The K_2O content of glauconite is an indication of the degree of glauconitization. On the basis of K_2O contents, glauconitic grains are divided into nascent (<4%), slightly evolved (4−6%), evolved (6−8%) and highly evolved (>8%) (Odin & Matter, 1981; Amorosi, 1995). In the present study, the K_2O contents of glauconite grains in sandstones and limestone are about 8%, corresponding to highly evolved materials. This is also confirmed by the high content of low-swelling layers in glauconite grains, which are represented by the well defined ~1 nm diffraction peak in XRD patterns, and the position of the Si–O absorption band in the IR spectra (near 1000 cm^{-1}; Figs 5 and 6).

The colour of glauconite grains is one of the most reliable indicators of glauconite maturity. During progressive glauconitization, the colour of glauconite changes from light green to dark green, induced by the enrichment of octahedrally coordinated Fe^{2+} relative to Fe^{3+} (Kuzmann *et al.*, 2008; Sánchez-Navas *et al.*, 2008). The high Fe^{2+}/TFe ratio (31%) in the glauconite from sample XL34 also indicates that the glauconite grains are highly evolved, as do their morphological characteristics.

Genesis of glauconite in the Xiala section: autochthonous or allochthonous?

Genesis of glauconite in sandstones. The use of glauconite in sequence stratigraphy requires an understanding of its genesis. Only autochthonous glauconite records the palaeo-environmental conditions of its development (Kazakov, 1983; Stille & Clauer, 1994; Amorosi, 1997). Previous studies have proposed many criteria for discriminating autochthonous from allochthonous glauconite (Bornhold & Giresse, 1985; Fischer, 1990; Amorosi, 1995, 1997; Huggett & Gale, 1997; Bandopadhyay, 2007).

Immature glauconite is a soft clay pellet, and transport over even short distances (several metres) can result in disaggregation. Highly fractured and highly evolved glauconite must have formed *in situ* (Huggett & Gale, 1997). The poor gradation and irregular morphology (notched, toothed or lacerated) indicate that the glauconite grains in the sandstones did not experience long-distance transport (Fig. 4a). We also observed the presence of deep fractures cutting completely across the grains, with the fractured pieces intact. We consider these observations to indicate an autochthonous origin of the glauconite in the sandstone layers. During glauconitization, the reduced volume of swelling layers in glauconite grains not only results in fractures at grain margins, but also in the development of pore spaces at the contact between glauconite and surrounding materials. Subsequently, calcite has precipitated in the shrinkage space.

Genesis of glauconite in limestone. Based on petrographic observations, the glauconite grains in limestone (sample XL35) are dispersed and concentrated in places, showing the same distribution characteristics as clastic quartz grains (Fig. 4e). These observations suggest that the glauconite grains were transported. As illustrated by the

EPMA data, the chemical variations in sandstone (sample XL34) and limestone (sample XL35) are similar with respect to the correlations between concentrations of ^{VI}Al and Fe^{3+} in glauconite grains, indicating that the glauconite grains in the limestone may have been derived from the underlying glauconitic sandstone (Fig. 7a).

The alteration of glauconite grains in the limestone is represented by leaching of Fe^{2+} from the octahedral layer of mature glauconite; the leached Fe^{2+} then oxidizes and precipitates as iron oxides which accumulate as particles or halos surrounding the glauconite grains. The EPMA data show a decrease in total Fe concentrations in glauconite grains within limestone relative to concentrations in sandstone (Table 2). The relative absorption intensities of OH-stretching vibration bands in the 3400–3700 cm^{-1} region also indicate a decrease of Fe_2O_3 and FeO concentrations in limestone relative to sandstone (Fig. 6). Thus, the glauconite grains in limestone appear to be allochthonous and altered.

Geological significance of autochthonous glauconite at Zanda

The process of glauconitization, involving the transformation of glauconitic precursor minerals to highly evolved glauconite, probably lasted about 1 m.y. (Odin & Fullagar, 1988; Garzanti, 1991). The presence of autochthonous, highly evolved glauconite at Zanda suggests that sedimentation rates in this area were low, with glauconitization likely to have occurred during a period of transgression.

During the Cretaceous, the Zanda area was located on the northern margin of the Indian continent and the palaeogeographic environment of the area greatly changed. The volcanic litharenite and quartz-arenite of the Gajie Formation (which underlies the glauconitic sandstone) were deposited in a delta-prodelta environment, whereas the limestone in the Bolinxiala Formation (above the glauconite-bearing condensed section) was deposited in a pelagic environment. Thus, the glauconite-bearing condensed section was deposited during an interval of increasing water depth. Indeed, Lower Cretaceous glauconite-bearing condensed sections, similar to those of the Gajie-Bolinxiala formations, have been reported at several localities on the northern margin of the palaeo-Indian continent, including Zanskar, Spiti, Thakkhola and Gamba (China) (Garzanti, 1993, 1999; Gibling *et al.*, 1994; Willems *et al.*, 1996; Li *et al.*, 2009; Hu *et al.*, 2010) (Fig. 1). It seems likely that the transgression was controlled by a single tectonic event, possibly related to the final separation of the Indian and Australian-Antarctic continents in the Late Albian.

Previous studies indicate that the separation of the Indian and Australian-Antarctic continents started in the Early Cretaceous (Powell *et al.*, 1988; Garzanti, 1993; Patzelt *et al.*, 1996). Hu *et al.* (2010) proposed that the unzipping of the Indian continent from the Australian-Antarctic continent was the result of counter-clockwise plate rotation, which resulted in the formation of deep-seated fractures that propagated northwestward along the northern margin of the Indian continent, coinciding with the deposits at Zanskar, Spiti, Zanda, Kumaon, Thakkhola and Gucuo (see fig. 10 in Hu *et al.*, 2010). Igneous activity related to this process is represented in the volcaniclastic materials that were transported and deposited in the sedimentary sequences found at these localities. The volcaniclastic source persisted until the Late Albian, which was the time of the final separation of the Indian and Australian-Antarctic continents. Subsequently, the Indian plate drifted northward, accompanied by the onset of subsidence of its northern margin due to thermal cooling of the crust. At Zanda, the simultaneous reduction in the supply of volcaniclastic and siliciclastic detritus, and a rise of sea level led to the formation of the transgressive condensed sequence. The highly evolved glauconite is consistent with this condensed sequence representing a period of time greater than that necessary to form mature glauconite, i.e. $>10^6$ years (Odin & Matter, 1981).

CONCLUSIONS

Cretaceous (Albian) sandstones and limestones of the Xiala section at Zanda, southwestern Tibet, China, contain highly evolved glauconite. The glauconite in the sandstones is autochthonous, whereas that in limestone was derived from the underlying glauconitic sandstone. Glauconitization may have been associated with the final separation of the Indian continent from the Australian-Antarctic continent in Late Albian time. After the separation, cooling of the Indian plate resulted in northward subsidence and subduction. The reduction in the supply of volcaniclastic and siliciclastic sediments, combined with a rise in sea level, led to

the formation of the transgressive sequence at Zanda. Continued transgression resulted in the evolution of the highly evolved glauconite minerals in this area.

ACKNOWLEDGMENTS

We thank W. Zhu for performing the FTIR spectroscopy analyses. We also thank J. Li and W.L. Zhang for help with the SEM and EPMA, respectively. This work was financially supported by the MOST 973 Project (2011CB822001, 2006CB701402) and the NSFC Project (40772070).

REFERENCES

Amorosi A. (1995) Glaucony and sequence stratigraphy: a conceptual framework of distribution in siliciclastic sequences. *Journal of Sedimentary Research*, **B65**, 419–425.

Amorosi A. (1997) Detecting compositional, spatial, and temporal attributes of glaucony: a tool for provenance research. *Sedimentary Geology*, **109**, 135–153.

Amouric M. & Parron C. (1985) Structure and growth mechanism of glauconite as seen by high-resolution transmission electron microscopy. *Clays and Clay Minerals*, **33**, 473–482.

Bandopadhyay P.C. (2007) Interpretation of authigenic vs. allogenic green peloids of ferric clay in the Proterozoic Penganga Group, southern India. *Clay Minerals*, **42**, 471–485.

Baum G.R. & Vail P.R. (1988) Sequence stratigraphic concepts applied to Paleogene outcrops, Gulf and Atlantic basins. Pp. 309–329 in: *Sea Level Changes-An Integrated Approach* (C.K. Wilgus, B.S. Hastings, C.G.St.C. Kendall, H.W. Posamentier, C.A. Ross & J.C. Van Wagoner, editors). SEPM Special Publication, vol. **42**. SEPM Society for Sedimentary Geology, Tulsa, USA.

Bédard É., Hébert R., Guilmette C., Lesage G., Wang C.S. & Dostal J. (2009) Petrology and geochemistry of the Saga and Sangsang ophiolitic massifs, Yarlung Zangbo Suture Zone, Southern Tibet: Evidence for an arc-back-arc origin. *Lithos*, **113**, 48–67.

Bentor Y.K. & Kastner M. (1965) Notes on the mineralogy and origin of glauconite. *Jourrnal of Sedimentary Petrology*, **35**, 155–166.

Berra F., Zanchi A., Mattei M. & Nawab A. (2007) Late Cretaceous transgression on a Cimmerian high (Neka Valley, eastern Alborz, Iran): A geodynamic event recorded by glauconitic sands. *Sedimentary Geology*, **199**, 189–204.

Bertle R.J. & Suttner T.J. (2005) New biostratigraphy data for the Chikkim Formation (Cretaceous, Tethyan Himalaya, India). *Cretaceous Research*, **26**, 882–894.

Besson G. & Drits V.A. (1997a) Refined relationship between chemical composition of dioctahedral fine-grained mica minerals and their infrared spectra within the OH stretching region. Part 1. Identification of the OH stretching vibrations. *Clays and Clay Minerals*, **45**, 158–169.

Besson G. & Drits V.A. (1997b) Refined relationship between chemical composition of dioctahedral fine-grained mica minerals and their infrared spectra within the OH stretching region. Part 2. Main factors affecting OH vibrations and quantitative analysis. *Clays and Clay Minerals*, **45**, 170–183.

Bornhold B.D. & Giresse P. (1985) Glauconitic sediments on the continental shelf off Vancouver Island, British Columbia, Canada. *Journal of Sedimentary Petrology*, **55**, 653–664.

Burst J.F. (1958a) 'Glauconite' pellets: their mineral nature and applications to stratigraphic interpretations. *Bulletin of the American Association of Petroleum Geologists*, **42**, 310–327.

Burst J.F. (1958b) Mineral heterogeneity in glauconite pellets. *Bulletin of the American Association of Petroleum Geologists*, **43**, 481–497.

Chen L., Hu X.M. & Huang Z.C. (2007) Constraints from Early Cretaceous volcaniclastic sandstones in southern Tibet on a volcanic event in the northern margin of the Indian continent. *Acta Geologica Sinica*, **81**, 501–510 (in Chinese).

Chen R.J. (1980) Characteristics of glauconites from some regions and their significance in analyzing the facies environment. *Scientia Geologica Sinica*, 65–79 (in Chinese).

Dèzes P. (1999) *Tectonic and Metamorphic Evolution of the Central Himalayan Domain in Southeast Zanskar (Kashmir, India)*. Ph.D. thesis, Institut de Mineralogie et Petrographie, Université de Lausanne, Switzerland.

Dubois-Côté V., Hébert R., Dupuis C., Wang C., Li Y. & Dostal J. (2005) Petrological and geochemical evidence for the origin of the Yarlung Zangbo ophiolites, southern Tibet. *Chemical Geology*, **214**, 265–286.

Dupuis C., Hébert R., Dubois-Côté V., Guilmette C., Wang C., Li Y. & Li Z. (2005a) The Yarlung Zangbo Suture Zone ophiolitic mélange (southern Tibet): new insights from geochemistry of ultramafic rocks. *Journal of Asian Earth Sciences*, **25**, 937–960.

Dupuis C., Hébert R., Dubois-Côté V., Wang C., Li Y. & Li Z. (2005b) Petrology and geochemistry of mafic rocks from melange and flysch units adjacent to the Yarlung Zangbo suture zone, southern Tibet. *Chemical Geology*, **214**, 287–308.

Dupuis C., Hébert R., Guilmette C., Wang C. & Li Z. (2006) Geochemistry of sedimentary rocks from mélange and flysch units south of the Yarlung

Zangbo Suture Zone, southern Tibet. *Journal of Asian Earth Sciences*, **26**, 489–508.

Eder V.G., Martin-Algarra A., Sánchez-Navas A., Zanin Y.N., Zamirailova A.G. & Lebedev Y.N. (2007) Depositional controls on glaucony texture and composition, Upper Jurassic, west Siberian basin. *Sedimentology*, **54**, 1365–1387.

Fischer H. (1990) Glauconite formation: discussion of the terms authigenic, perigenic, allogenic, and metaallotenic. *Eclogae Geologicae Helvetiae*, **83**, 1–6.

Garzanti E. (1991) Non-carbonate intrabasinal grains in arenites: their recognition, significance and relationship to eustatic cycles and tectonic setting. *Journal of Sedimentary Petrology*, **61**, 959–975.

Garzanti E. (1993) Sedimentary evolution and drowning of a passive margin shelf (Giumal Group; Zanskar Tethys Himalaya, India): palaeoenvironmental changes during final break-up of Gondwanaland. *Geological Society, London, Special Publications*, **74**, 277–298.

Garzanti E. (1999) Stratigraphy and sedimentary history of the Nepal Tethys Himalaya passive margin. *Journal of Asian Earth Sciences*, **17**, 805–827.

Gibling M.R., Gradstein F.M., Kristiansen I.L., Nagy J., Sarti M. & Wiedmann J. (1994) Early Cretaceous strata of the Nepal Himalayas: conjugate margins and rift volcanism during Gondwanan breakup. *Journal of the Geological Society of London*, **151**, 269–290.

Guo T., Liang D., Zhang Y. & Zhao C. (1991) *Ali Geology*. The China University of Geosciences Press, Wuhan, 1–464 (in Chinese).

Hébert R., Huot F., Wang C. & Liu Z. (2003) Yarlung Zangbo ophiolites, southern Tibet revisited: geodynamic implications from the mineral record. Pp. 165–190 in: *Ophiolites in Earth History* (Y. Dilek & P.T.Robinson, editors). *Journal of the Geological Society, London Special Publication*, **218**.

Hodges K.V. (2000) Tectonics of the Himalaya and southern Tibet from two perspectives. *Geological Society of America Bulletin*, **112**, 324–350.

Hodges K.V., Parrish R.R. & Searle M.P. (1996) Tectonic evolution of the central Annapurna Range, Nepalese Himalayas. *Tectonics*, **15**, 1264–1291.

Hu X., Jansa L. & Wang C. (2008) Upper Jurassic–Lower Cretaceous stratigraphy in southeastern Tibet: a comparison with the western Himalayas. *Cretaceous Research*, **29**, 301–315.

Hu X.M., Jansa L., Chen L., Griffin W.L., O'Reilly S.Y. & Wang J.G. (2010) Provenance of Lower Cretaceous Wölong volcaniclastics in the Tibetan Tethyan Himalaya: Implications for the final breakup of eastern Gondwana. *Sedimentary Geology*, **223**, 193–205.

Huggett J.M. & Gale A.S. (1997) Petrology and palaeoenvironmental significance of glaucony in the Eocene succession at Whitecliff Bay, Hampshire Basin, U.K. *Journal of the Geological Society of London*, **154**, 897–912.

Huggett J.M., Gale A.S. & McCarty D. (2010) Petrology and Palaeoenvironmental significance of authigenic iron-rich clays, carbonates and apatite in the Claiborne Group, Middle Eocene, NE Texas. *Sedimentary Geology*, **228**, 119–139.

Jadoul F., Berra F. & Garzanti E. (1998) The Tethys Himalayan passive margin from late Triassic to early Cretaceous (South Tibet). *Journal of Asian Earth Sciences*, **16**, 173–194.

Jiménez-Millán J. & Castro J.M. (2008) K-feldspar alteration to gel material and crystallization of glauconitic peloids with berthierine in Cretaceous marine sediments – sedimentary implications (Prebetic Zone, Betic Cordillera, SE Spain). *Geological Journal*, **43**, 19–31.

Kazakov G.A. (1983) Glauconites as indicators for geochemical sediment formation conditions. *Geochemistry International*, **20**, 129–139.

Kelly J.C. & Webb J.A. (1999) The genesis of glaucony in the Oligo-Miocene Torquay Group, southeastern Australia: petrographic and geochemical evidence. *Sedimentary Geology*, **125**, 99–114.

Kuzmann E., Weiszburg T.G., Toth E. & Garg V.K. (2008) Mössbauer characteristics of glauconitisation. *Hyperfine Interactions*, **186**, 1–8.

Li G.B., Jiang G.Q., Hu X.M. & Wan X.Q. (2009) New biostratigraphic data from the Cretaceous Bolinxiala Formation in Zanda, southwestern Tibet of China, and their paleogeographic and paleoceanographic implications. *Cretaceous Research*, **30**, 1005–1018.

Liu G. & Einsele G. (1994) Sedimentary history of the Tethyan basin in the Tibetan Himalayas. *Geologische Rundschau*, **83**, 32–61.

Loutit T.S., Hardenbol J. & Vail P.R. (1988) Condensed sections: the key to age determination and correlation of continental margin sequences. Pp. 183–213 in: *Sea Level Changes – An Integrated Approach*. (C.K. Wilgus, B.S. Hastings, C.G.St.C. Kendall, H.W. Posamentier, C.A. Ross & J.C. Van Wagoner, editors). *SEPM Special Publication*, **42**. SEPM Society for Sedimentary Geology, Tulsa, USA.

McRae S.G. (1972) Glauconite. *Earth Science Reviews*, **8**, 397–440.

Manghnani M.H. & Hower J. (1964) Glauconites: cation exchange capacities and infrared spectra, Part II. *American Mineralogist*, **49**, 1631–1642.

Odin G.S. & Fullagar P.D. (1988) Geological significance of the glaucony facies. Pp. 295–332 in: *Green Marine Clays* (G.S. Odin, editor). Developments in Sedimentology, **45**, Elsevier, Amsterdam.

Odin G.S. & Matter A. (1981) De glauconiarum origine. *Sedimentology*, **28**, 611–641.

Odom E.I. (1976) Microstructure, mineralogy and chemistry of Cambrian glauconite pellets and

glauconite, central U.S.A. *Clays and Clay Minerals*, **24**, 232–238.

Odom E.I. (1984) Glauconite and celadonite minerals. Pp. 545–584 in: *Micas* (S.W. Bailey, editor). Review in Mineralogy, **13**, Mineralogical Society of America, Chantilly, USA.

Patzelt A., Li H., Wang J. & Appel E. (1996) Palaeomagnetism of Cretaceous to Tertiary sediments from southern Tibet: evidence for the extent of the northern margin of India prior to the collision with Eurasia. *Tectonophysics*, **259**, 259–284.

Posamentier H.W., Jervey M.T. & Vail P.R. (1988) Eustatic controls on clastic deposition. I. Conceptual framework. Pp. 110–124 in: *Sea Level Changes – An Integrated Approach* (C.K. Wilgus, B.S. Hastings, C.G.St.C. Kendall, H.W. Posamentier, C.A. Ross & J.C. Van Wagoner, editors). *SEPM Special Publication*, **42**. SEPM Society for Sedimentary Geology, Tulsa, USA.

Powell C.M., Roots S.R. & Veevers J.J. (1988) Prebreakup continental extension in East Gondwanaland and the early opening of the eastern Indian Ocean. *Tectonophysics*, **155**, 261–283.

Sánchez-Navas A., Martin-Algarra A., Eder V., Reddy B.J., Nieto F. & Zanin Y.N. (2008) Color, mineralogy and composition of Upper Jurassic west Siberian glauconite: usefull indicators of paleoenvironment. *The Canadian Mineralogist*, **46**, 1249–1268.

Sinha A. (1989) *Geology of the Higher Central Himalaya.* John Wiley and Sons, New York, 219 pp.

Slonimskaya M.V., Besson G., Dainyak L.G., Tchoubar C. & Drits V.A. (1986) Interpretation of the IR spectra of celadonites and glauconites in the region of OH-stretching frequencies. *Clay Minerals*, **21**, 377–388.

Stille P. & Clauer N. (1994) The process of glauconitization: chemical and isotopic evidence. *Contributions to Mineralogy and Petrology*, **117**, 253–262.

Thompson R. & Hower J. (1975) The mineralogy of glauconite. *Clays and Clay Minerals*, **23**, 289–300.

Vail P.R., Hardenbol J. & Todd R.G. (1984) Jurassic unconformities; Chronostratigraphy, and sea-level changes from seismic stratigraphy and biostratigraphy. Pp. 1129–1144 in: *Interregional Unconformities and Hydrocarbon Accumulation* (I.S. Schlee, editor). American Association of Petroleum Geologists Memoir, **36**, AAPG, Tulsa, USA.

Van Wagoner J.C., Mitchum R.M., Campion K.M. & Rahmanian V.D. (1990) Siliciclastic Sequence Stratigraphy in Well Logs, Cores, and Outcrops: *American Association of Petroleum Geologists Methods in Exploration Series*, no.**7**, 55 pp.

Wiewióra A., Giresse P., Petit S. & Wilamowski A. (2001) A deep-water glauconitization process on the Ivory Coast-Ghana marginal ridge (ODP site 959): determination of Fe^{3+}-rich montmorillonite in green grains. *Clays and Clay Minerals*, **49**, 540–558.

Willems H., Zhou Z., Zhang B. & Grafe K.U. (1996) Stratigraphy of the Upper Cretaceous and Lower Tertiary strata in the Tethyan Himalayas of Tibet (Tingri area, China). *Geologische Rundschau*, **85**, 723–754.

Zhang N.X. (1981) The mineralogical study of glauconites from some regions of China. *Scientia Geologica Sinica*, 376–383 (in Chinese).